Carriage interior noise-based inspection for rail corrugation on high-speed railway track

Wei, Zilong; Sun, Xianfu; Yang, Fei; Ke, Zaitian ; Lu, Tao; Zhang, Pan; Shen, Chen

DOI
10.1016/j.apacoust.2022.108881

Publication date
2022

Document Version
Final published version

Published in
Applied Acoustics

Applied Acoustics 196 (2022) 108881

Contents lists available at ScienceDirect

Applied Acoustics

journal homepage: www.elsevier.com/locate/apacoust

Carriage interior noise-based inspection for rail corrugation on high-speed railway track

Zilong Wei [a], Xianfu Sun [a], Fei Yang [a,*], Zaitian Ke [a], Tao Lu [b], Pan Zhang [c], Chen Shen [c]

[a] Infrastructure Inspection Research Institute, China Academy of Railway Sciences, No. 2 Daliushu Road, Haidian District, Beijing, China
[b] MOE Key Laboratory of High-Speed Railway Engineering, Southwest Jiaotong University, No. 111, North Section 1, Second Ring Road, Chengdu, China
[c] Section of Railway Engineering, Faculty of Civil Engineering and Geosciences, Delft University of Technology, Stevinweg 1, 2628 CN, Delft, the Netherlands

ARTICLE INFO

Article history:
Received 25 April 2022
Received in revised form 23 May 2022
Accepted 13 June 2022

Keywords:
Carriage interior noise
Rail corrugation
High-speed railway
Acoustic inspection

ABSTRACT

The presence of rail corrugation enlarges the wheel-rail impact and exacerbates the failure of track components, and the situation becomes even worse under high train speed, which promotes the urgent need for an efficient and easily accessible inspection method. Conventional diagnosis approaches such as axle box acceleration (ABA) and image recognition measurements, however, require complex instrumentations on the running gear, restricting their applications on a wide range of operational trains. In this study, we investigate the capability of carriage interior noise in diagnosing rail corrugation on the high-speed railway (HSR). For this purpose, train-borne vibration & noise measurements were integrated with in-situ rail surface irregularity tests, to extract the characteristic carriage interior responses induced by rail corrugation. The measurements were conducted on two HSR tracks with different corrugation geometries, and the time–frequency distributions of interior noise were identified under different train speeds and with different track radii. Afterward, an interior noise-based inspection algorithm was proposed by proper correlation of the gained data, and was then demonstrated on a third HSR track with an unknown rail surface condition. The comparison between the proposed inspection algorithm and the widely-recognized ABA measurements indicates that the interior noise succeeded in identifying the position, typical wavelength and severity of rail corrugation under varying train speeds. The work advances a cost-effective and easily accessible way for the condition monitoring of railway tracks.

1. Introduction

Rail corrugation, characterized by an irregular sequence of ridges and dark hollows on the running surface [1], is one of the major rail defects. The presence of rail corrugation enlarges the wheel/rail contact forces, induces undesired vibrations & noises, and speeds up the deterioration of vehicle and track components [2–6]. On HSR tracks, rail corrugation (e.g., the examples shown in Fig. 1) would further aggravate wheel/rail impact under high train speed, and even endanger the safety and stability of railway operation [7]. Therefore, it is of importance to inspect rail corrugation efficiently, so that maintenance actions such as rail grinding can be conducted in a timely fashion.

In the railway industry, the methods capable of inspecting rail corrugation can be classified into two categories, i.e., the foldable trolley and the train-borne equipment. The foldable trolley can measure the rail surface irregularity with a dense sampling interval, e.g., 1 ~ 2 mm for the well-known Corrugation Analysis Trolley (CAT) [8]. Yet, the inspection speed of foldable trolleys is commonly limited to 1 ~ 2 m/s, so a substantial number of man-hours are required for large-scale railway networks. The train-borne equipment provides an alternative way to diagnose rail anomalies efficiently. The principle employed by the train-borne equipment includes image recognition [9], on-board contact measurement [8], ABA measurement [10], laser imaging [11,12], and so on. The image recognition method can identify visible anomalies on rail surfaces, yet it often lacks accuracy when measuring the depth of irregularities [13]. On-board contact measurement, similar to the portable trolley, can measure the geometry of rail surface irregularity directly. Yet, the inspection speed of on-board contact measurement is limited, e.g., up to 15 km/h on reprofiling trains and 55 km/h on hi-rail vehicles [14], which restricts its application on high-speed trains. The laser imaging measurement can be conducted at train operational speed, whereas its performance may be affected by illumination inequality and contaminations on rail

* Corresponding author.
E-mail addresses: weizilong@rails.cn (Z. Wei), sunxianfu@rails.cn (X. Sun), 13811807268@163.com (F. Yang), kezt@rails.cn (Z. Ke), t.lyu@swjtu.edu.cn (T. Lu), P.Zhang@tudelft.nl (P. Zhang), C.Shen-2@tudelft.nl (C. Shen).

https://doi.org/10.1016/j.apacoust.2022.108881
0003-682X/

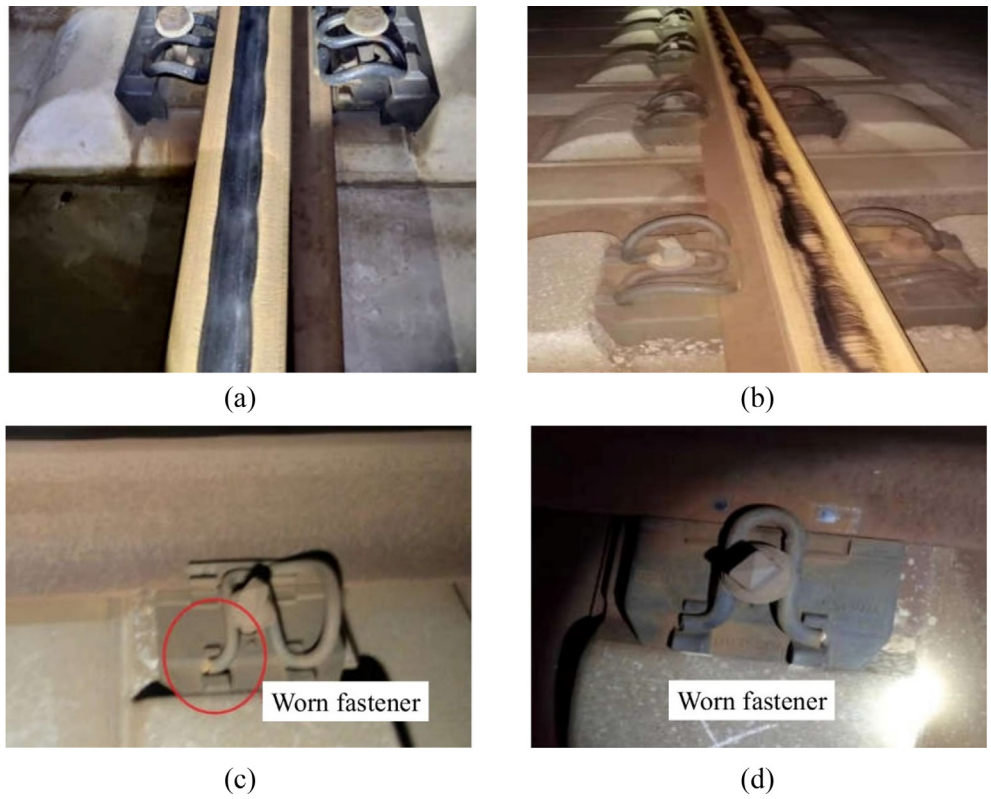

Fig. 1. Examples of rail corrugation on HSR lines: (a) Sharp curve, (b) Tangent track, (c) and (d) Failure of the fastener at track sections with rail corrugation.

surfaces. ABA measurement can identify defects on both rail surface [15,16] and other track components (e.g., loose bolts and worn railpads [17]), the sensors need to be installed on the running gear of vehicles. Due to safety issues, some authorities of the HSR network (e.g., in China) is very cautious to instrument sensors outside of the train carriage, which restrict its application on a wide range of operational trains. Alternatively, by arranging compact sensors inside the cabinet of railway vehicles, the carriage interior response measurement provides a cost-effective and easy-to-operate way for the condition monitoring of railway tracks [18]. For example, the smartphone is used for evaluating the ride comfort of railway tracks [19–21], while the microphone is used for evaluating the performance of rail grinding [22,23]. Yet, these attempts were almost made on railway lines with operation speeds no higher than 160 km/h, and the main efforts are almost paid to the overall quality of railway tracks rather than specific track defects.

In this study, we investigate the capability of the carriage interior noise in inspecting rail corrugation on HSR tracks. For this purpose, in-situ rail surface irregularity tests and train-borne vibration & noise measurements were conducted on two HSR tracks with different curve radii, train speeds and corrugation geometries. The characteristics of carriage interior responses induced by rail corrugation were extracted, and they were employed to design the diagnosis algorithm of rail corrugation. The proposed algorithm was then demonstrated on a third HSR track with an unknown rail surface condition, and the results were verified using the widely-recognized ABA measurements. Fig. 2 shows the structure of the methodology. We expect that the results will not only enhance our understanding of the corrugation-induced vehicle/track interaction on HSR tracks but also advance a high-efficient and easily-accessible way for the inspection of rail corrugation.

The paper is organized as follows. Section 2 illustrates the setup of the train-borne measurements. Section 3 analyzes the characteristics of carriage interior vibrations and noises induced by rail corrugation on two HSR tracks with different curve radii and train speeds, and the time–frequency distributions of the interior noise are compared in detail with the ABA signals. Section 4 proposes an interior noise-based inspection algorithm, and demonstrates its capability on a third HSR track with an unknown rail surface condition. Finally, Section 5 draws the main conclusions and further work.

2. Setup of train-borne and in-situ measurements

2.1. Train-borne measurements of carriage interior responses

The train-borne measurements were conducted in the tourist cabin of a CRH380B-type high-speed train, see Fig. 2. Since the pantograph was not installed on the roof of the first carriage, the disturbances of the pantograph-induced aerodynamic noise [24] can be excluded. The carriage interior instrument includes four main components, i.e., an accelerometer, a MEMS Global Navigation Satellite System (GNSS)/ Inertial Navigation System (INS) integrated navigation system, a signal acquisition device, and a microphone. The sensors were mounted on the carriage floor above the leading bogie and close to the driver's cage. Among them, the accelerometer is employed for recording the acceleration of the car body, while the microphone for the noise inside the carriage, and the sampling frequency of both sensors were set to 5 kHz. The GNSS/INS integrated navigation system was employed to record the position and speed of the measurement train. In particular, the GNSS antenna was arranged next to a side window, while the INS module was triggered when the GNSS signal is poor (e.g., within train station and tunnel). Apart from the sensors inside the carriage, an accelerometer with a sampling frequency of 5 kHz was also installed on the axle box of the leading bogie of the first

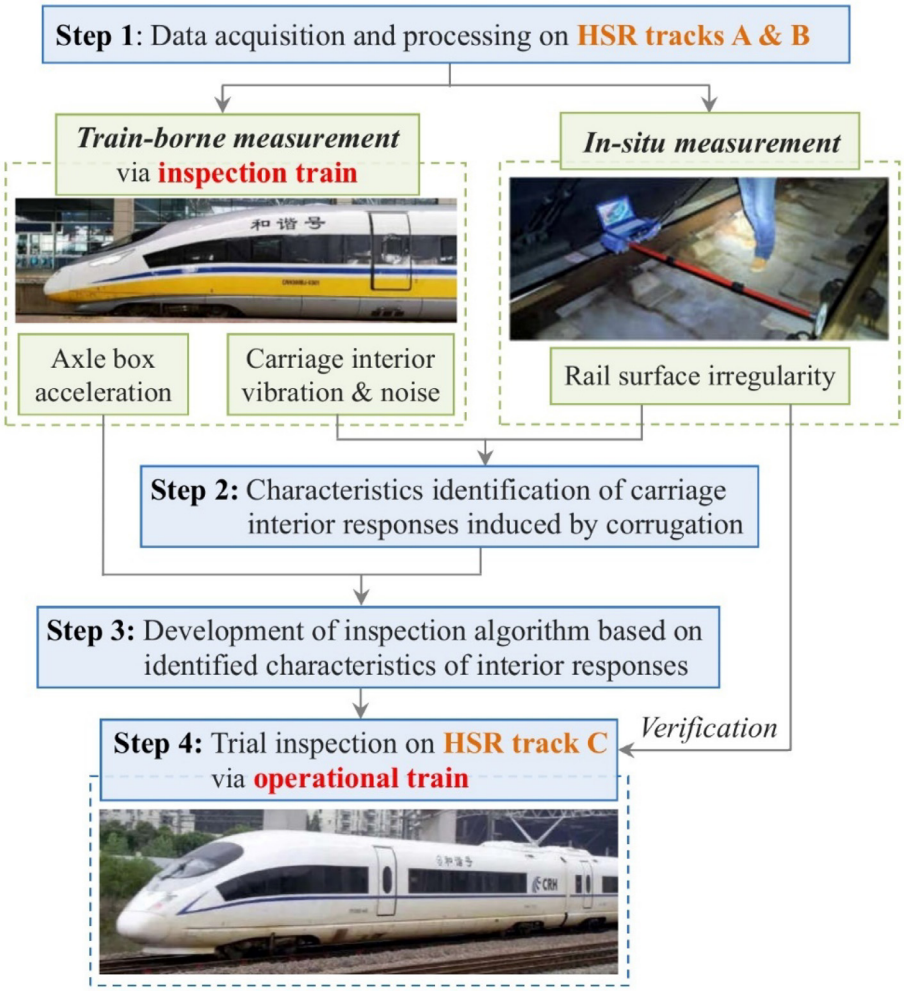

Fig. 2. Flow chart depicting the methodology in this study.

carriage (see Fig. 3(c)), so that the dynamic responses of running gear components can be extracted.

The vibration and noise signals were recorded in the time domain. To extract the detailed time–frequency distributions of the measured signals, the synchrosqueezed transform (SST) algorithm [25,26] is employed. Compared with short-time Fourier transform (STFT) and continuous wavelet transform (CWT), the SST algorithm promotes the signal energy concentration around the instantaneous frequencies without affecting the time resolution. Therefore, the SST algorithm improves the sharpness of the signal analysis in the frequency direction and is more suitable for extracting the oscillatory components from vibration and noise signals.

For an input signal$s(t)$, the wavelet coefficients $W_s(a,b)$ based on CWT are expressed as:

$$W_s(a,b) = \frac{1}{\sqrt{a}} \int_{-\infty}^{\infty} s(t)\, \psi\left(\frac{t-b}{a}\right)\, dt \tag{1}$$

where a is the wavelet scale, b is the time step. ψ is the mother wavelet, and the Morlet function [27] was employed in this study.

In the scenario satisfying$W_s(a,b)\neq 0$, a candidate instantaneous frequency can then be calculated via the following phase transform:

$$\omega_s(a,b) = \frac{-i}{2\pi W_s(a,b)} \frac{\partial W_s(a,b)}{\partial b} \tag{2}$$

The information from the time-scale plane is then transferred to the time–frequency plane. Assuming no confusion occurs, the dependence on s is suppressed and simplified as$\omega(a,b)$. For the discrete values a andω, the synchrosqueezed transform $T_s(\omega,b)$ of $W_s(a,b)$ is expressed as:

$$T_s(\omega_l,b) = \frac{1}{\Delta\omega} \sum_{a_k:|\omega(a_k,b)-\omega_l|\leq\Delta\omega/2} \left(W_s(a_k,b)a_k^{-3/2}\Delta a_k\right) \tag{3}$$

where a_k and ω_l are discrete values of a and ω. Δa_k and $\Delta\omega$ are step sizes, satisfying $\Delta a_k = a_k - a_{k-1}$ and $\Delta\omega = \omega_l - \omega_{l-1}$.

On this basis, two indexes, namely the global wavelet power spectrum (GWPS) and scale-averaged wavelet power (SAWP), are employed to extract improved quantification of the WPS distributions. Among them, the GWPS can quantify the distributions of WPS at each frequency, expressed as:

$$G_s(\omega_l) = \frac{1}{N_G} \sum_{n=0}^{N-1} |T_s(\omega_l,b_n)|^2 \tag{4}$$

where N_G is the total number of sampling points within the specified period.

The SAWP is defined as the weighted sum of the WPS in the frequency band f_1 to f_2 [28]:

$$T_s[f_1,f_2] = \frac{1}{N_S} \sum_{l=l_1}^{l_2} |T_s(\omega_l,b)|^2 \tag{5}$$

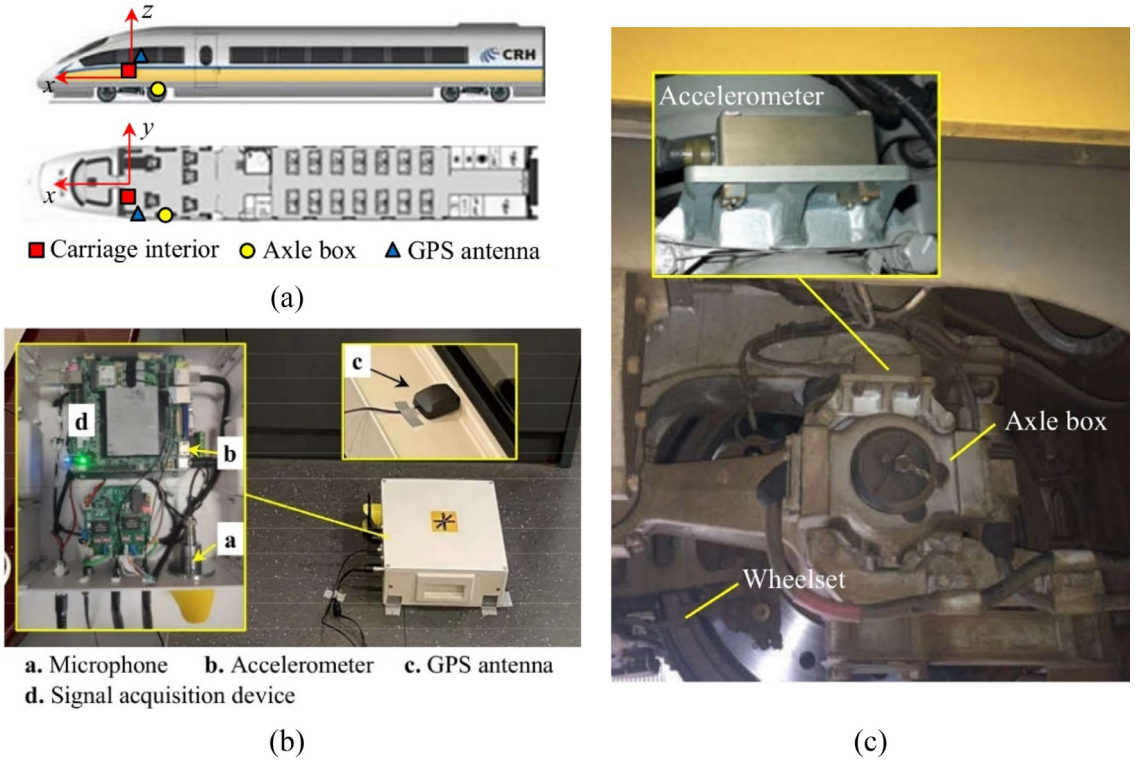

Fig. 3. Schematic diagram of train-borne measurement. (a) Instrumented position of sensors, (b) Singal acquisition device, and (c) Accelerometer mounted on axle box.

where N_S is the total number of sampling points within the specified frequency band f_1 tof_2, while l_1 and l_2 are the sequence number of f_1 tof_2.

2.2. In-situ measurement of rail surface irregularity

In-situ measurements of rail surface irregularity were conducted using the portable trolley CAT, as shown in Fig. 1. During the measurement, the irregularity along the centerline of the running band was recorded, and the sampling interval s_r was set to 1 mm. To extract the position, typical wavelength, and severity of rail corrugation, the measured rail surface irregularity is evaluated using the indexes of roughness level and moving average of root-mean-square (RMS) amplitude. According to Standard ISO 3095:2013 [29], the roughness level L_r of the rail surface is expressed as:

$$L_r = 10\lg\left(\frac{r_{\mathrm{RMS}}}{r_0}\right)^2 \tag{6}$$

where L_r is the roughness level in dB, r_{RMS} is the RMS roughness in μm, and r_0 is the reference roughness and equals 1 μm.

According to Standard EN 13231–3:2006 [30], the moving average RMS of digitally represented rail irregularity (with values of$y(x)$,$y(x+\Delta x)$,…, $y(x+n\Delta x)$) locating in a specified window with length of L can be expressed as:.r_{RMS}

$$V_{\mathrm{RMS}}(x) = \sqrt{\frac{1}{n-1}\sum_{i=1}^{n} y^2(x)} \tag{7}$$

where n is the number of irregularity samples, calculated from$n = L/s_r$.

The values of L in Standard EN 13231–3:2006 are specified as 0.15 m, 0.5 m, 1.5 m, and 5.0 m for the wavelength ranges of 10 ∼ 30 mm, 30 ∼ 100 mm, 100 ∼ 300 mm, and 300 ∼ 1000 mm, respectively.

3. Characteristic carriage interior responses induced by corrugation on HSR

In this section, both the train-borne and in-situ measurements were conducted on two HSR tracks with rail corrugation. The vehicle responses in terms of vertical car body acceleration (CBA), carriage interior noise, and vertical axle box acceleration (ABA) were recorded, and their relation with the measured rail surface irregularities is investigated. Between the two tracks, both the curve radius and train speed differ significantly, so that the time–frequency characteristics of carriage interior responses under different scenarios can be identified.

3.1. Characteristics of carriage interior responses

In the HSR network, there exist sharp curves around many railway stations, at which rail corrugation commonly has a high likelihood to initiate and develop [31]. Fig. 4 gives examples of rail corrugation occurring on the transition curve of a sharp curve of the HSR track A. In the figure, the rail corrugation can be observed on both the inner and outer rails. The transition curve is with a minimum radius R of 1600 m, and the train measurement speed is around 110 km/h.

Fig. 5 shows the distribution of rail surface irregularity measured on the sharp curve of the HSR track A. Regarding the roughness level in Fig. 5(a), the values at the 1/3 octave wavelength of 63 mm are 20.3 dB on the inner rail and 16.4 dB on the outer rail, both of which exceed the limit of 0.9 dB according to Standard ISO 3095:2013. The power spectrum of the rail irregularity in Fig. 5(b) further indicates that the wavelength of 58 mm is dominant on both rails. To clearly illustrate the geometric characteristics of rail corrugation, the measured data is filtered with the passband of 30 ∼ 100 mm following Standard EN 13231-3:2006, and the results are given in Fig. 5(c)∼(d). On the inner rail, the peak-to-peak value (V_{PP}) of filtered rail irregularity exceeds 30 μm at 63 ∼ 104 m,

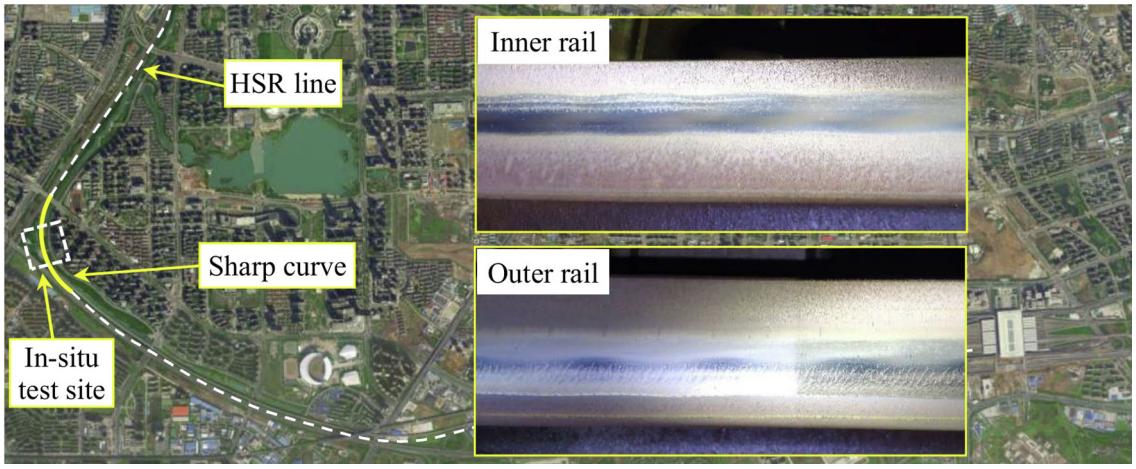

Fig. 4. Rail corrugation on the sharp curve of the HSR track A.

118 ~ 173 m, and 177 ~ 189 m, with the maximum of 101 μm occurring at $x = 134$ m. On the outer rail, the V_{PP} exceeds 30 μm at 68 ~ 92 m, 115 ~ 152 m, and 167 ~ 204 m, with the maximum of 58 μm occurring at $x = 126$ m. Fig. 5(e)-(f) shows the moving average RMS of the filtered rail surface irregularity with the passband of 30 ~ 100 mm. As can be seen, the values of V_{RMS} reach the maxima of 31.5 μm on the inner rail and 17.4 μm on the outer rail. Judged by the threshold of 4 μm according to Standard EN 13231-3:2006, 75.2% and 42.3%of the in-situ measured track section (i.e., 400 m) exceeds the limit on the inner rail and outer rail, respectively.

Fig. 6 shows the time and frequency distributions of the carriage interior responses on the sharp curve. In Fig. 6(a)-(b), large energy concentrations in the frequency range of 500 ~ 550 Hz can be observed from both the CBA and noise signals. Since the typical wavelength of the rail surface irregularity is 58 mm, the corrugation-induced vehicle responses should tack place at around 527 Hz under the train speed of 110 km/h. This indicates that the 500 ~ 550 Hz components are strongly correlated with the excitation of rail corrugation.

To gain an insight into the relationship between the severity of rail corrugation and the energy of carriage interior responses, three sites, namely A1 ($x = 16$ m), A2 ($x = 134$ m) and A3 ($x = 350$ m) are picked up from Fig. 5(e), with the amplitudes of V_{RMS} being 3.7 μm, 31.5 μm, and 3.2 μm on the inner rail, respectively. Fig. 6(c)-(d) compares the GWPS of the carriage interior responses at the sites. For both the CBA and interior noise signals, the power spectrum at 500 ~ 550 Hz raises with the exacerbation of rail corrugation. The GWPS of the interior noise in Fig. 6(d) is 4.4×10^{-3} Pa^2 and 3.6×10^{-3} Pa^2 at A1 and A3 respectively, where the corrugation amplitudes are similar between the two sites, and the value increases to 1.5×10^{-2} Pa^2 at A2. Regarding the GWPS of the CBA, however, the values at A1 and A3 (e.g., 6.2×10^{-3} m^2/s^4 and 2.8×10^{-3} m^2/s^4) differ significantly from each other, indicating its poor correlation with the corrugation amplitude.

Fig. 7 gives another example of rail corrugation on a large curve of the HSR track B. The degraded track section is within a tunnel of HSR track B, the curve radius is 10000 m, and the measurement speed is around 300 km/h.

Fig. 8 shows the rail surface irregularity measured on the HSR track B. The roughness level at the 1/3 octave wavelength of 125 mm reaches 13.0 dB on the inner rail and 10.1 dB on the outer rail (Fig. 8(a)), both of which exceed the limit of 7.0 dB according to Standard ISO 3095:2013. Regarding the power spectrum of the measured irregularity, the typical wavelength is 141 mm on both rails, see Fig. 8(b). Fig. 8(c)-(d) gives the rail surface irregularity bandpass filtered in the range of 100 ~ 300 mm. As can be seen, the maximum of the V_{PP} is 81 μm at $x = 40$ m of the inner rail, which reduces to 52 μm at $x = 134$ m of the outer rail. Fig. 8(e)-(f) shows the moving average RMS of the filtered rail surface irregularity with the passband of 100 ~ 300 mm. Along the in-situ measured length of 400 m, 5.6% of the V_{RMS} on the inner rail exceeds the threshold of 12 μm according to Standard EN 13231–3:2006, while the ratio reduces to 0.7% on the outer rail.

Fig. 9 shows the time and frequency distributions of the carriage interior responses recorded on the HSR track B. Since the typical wavelength of rail surface irregularity is 141 mm, the induced vibrations and noises are most likely to take place at around 591 Hz under the train speed of 300 km/h. In Fig. 9(a)-(b), however, the 550 ~ 650 Hz components can be hardly observed from both the CBA and interior noise. This is mainly attributed to the great energy concentration at lower frequencies (e.g., 30 ~ 100 Hz), which makes the higher frequency components unimpressive under the same scale. To investigate the relationship between the severity of rail corrugation and the energy of carriage interior responses, three sites with different irregularity amplitudes, namely B1 ($x = 40$ m), B2 ($x = 150$ m) and B3 ($x = 274$ m), are picked up from Fig. 8(e), with the amplitudes of V_{RMS} being 16.6 μm, 8.7 μm, and 8.0 μm on the inner rail, respectively. Fig. 9(c)-(d) compares the GWPS of the carriage interior responses at the three sites. As can be seen, the exacerbation of rail corrugation promotes the energy concentration of the interior noise at around 600 Hz, see Fig. 9(d). In particular, the value of GWPS at B1 is 52% and 56% larger than those at B2 and B3. Regarding the GWPS of the CBA signal, the power spectrum at 550 ~ 650 Hz is not significant compared to the values nearby, and it does not raise at a larger corrugation amplitude, which may have been effectively isolated by the suspensions.

3.2. Comparison of carriage interior responses with ABA

In the literature, the ABA measurements have been intensively demonstrated for the diagnosis of rail corrugation [15]. In this study, the ABA is employed to examine the time–frequency characteristics of the carriage interior responses induced by rail corrugation. On the HSR tracks A and B, both the ABA and carriage interior responses were captured using the inspection train, and their instrumented positions are close to each other along the longitudinal direction (see Fig. 3). Fig. 10 shows the distributions of the vertical ABA measured using the high-speed inspection train (see

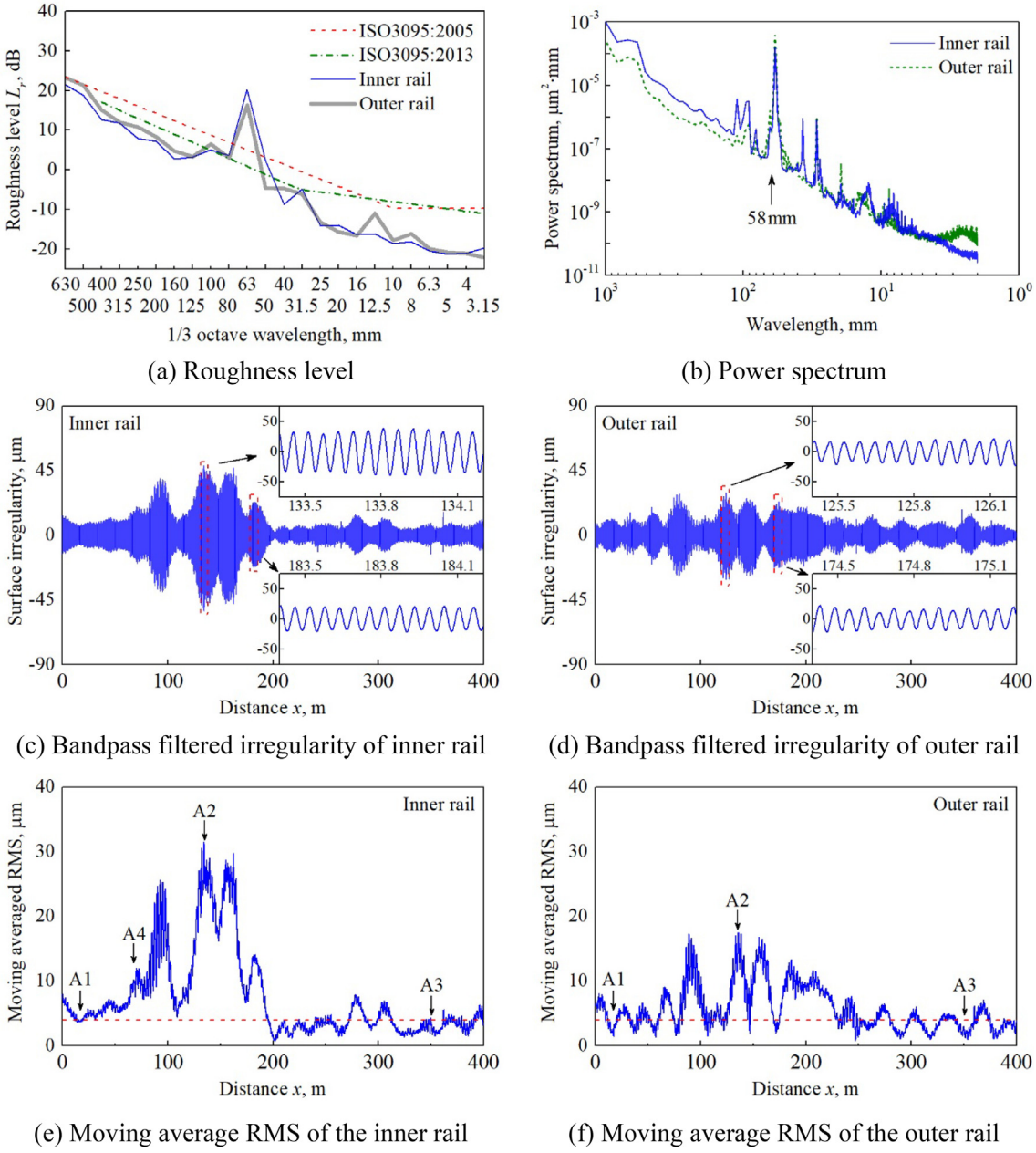

Fig. 5. Rail surface irregularity on the sharp curve of the HSR track A.

Fig. 2). On the HSR track A, the presence of rail corrugation promotes energy concentration at 500 ~ 550 Hz (Fig. 10(a)), and the power spectrum at the three selected sites A1 ~ A3 (Fig. 5(e)) raises with the exacerbation of rail corrugation (Fig. 10(c)). A similar phenomenon also takes place on the HSR track B, at which the great vibration energy at 550 ~ 650 Hz (Fig. 10(b)) is mainly attributed to the excitation of rail corrugation. Besides, some other frequency components can be picked up from the ABA signals, e.g., those at 300 ~ 350 Hz and 1000 ~ 1050 Hz in Fig. 10(a). These components are not clearly observed from the CBA signal, which should be effectively isolated by the suspensions.

Fig. 11 shows the SAWP extracted from different vehicle response signals. In the figure, the concerned frequencies are restricted to 500 ~ 550 Hz for the HSR track A and 550 ~ 650 Hz for the HSR track B, respectively. For comparison purposes, the SAWP is normalized by dividing its mean value along the whole measured length. On the HSR track A, both the CBA and interior noise coincide well with the ABA signals in terms of both the waveform and amplitude, see Fig. 11(a). The maxima of the SAWP take place at around $x = 994.20$ km for all the measured signals, with the normalized values being 13.8, 12.3, and 14.9 for the CBA, interior noise, and ABA, respectively. This information indicates that both of the two measured carriage interior response signals succeed in capturing the region with rail corrugation.

On the HSR track B, the SAWP of the interior noise and ABA signals shows a good approximation in terms of the waveform, with the maxima of both signals occurring at around $x = 842.85$ km. Note that the SAWP of the interior noise within the tunnel is higher than the adjacent regions [32,33], while the phenomenon is not obvious for the ABA and CBA signals. The maximum SAWP of the CBA takes place at $x = 843.75$ km, shifting forward by 0.9 km compared with the ABA. As shown in Fig. 9(c) and Fig. 11(b), the CBA measured from the HSR track B fails in capturing both the characteristic frequency components and the exact position of rail

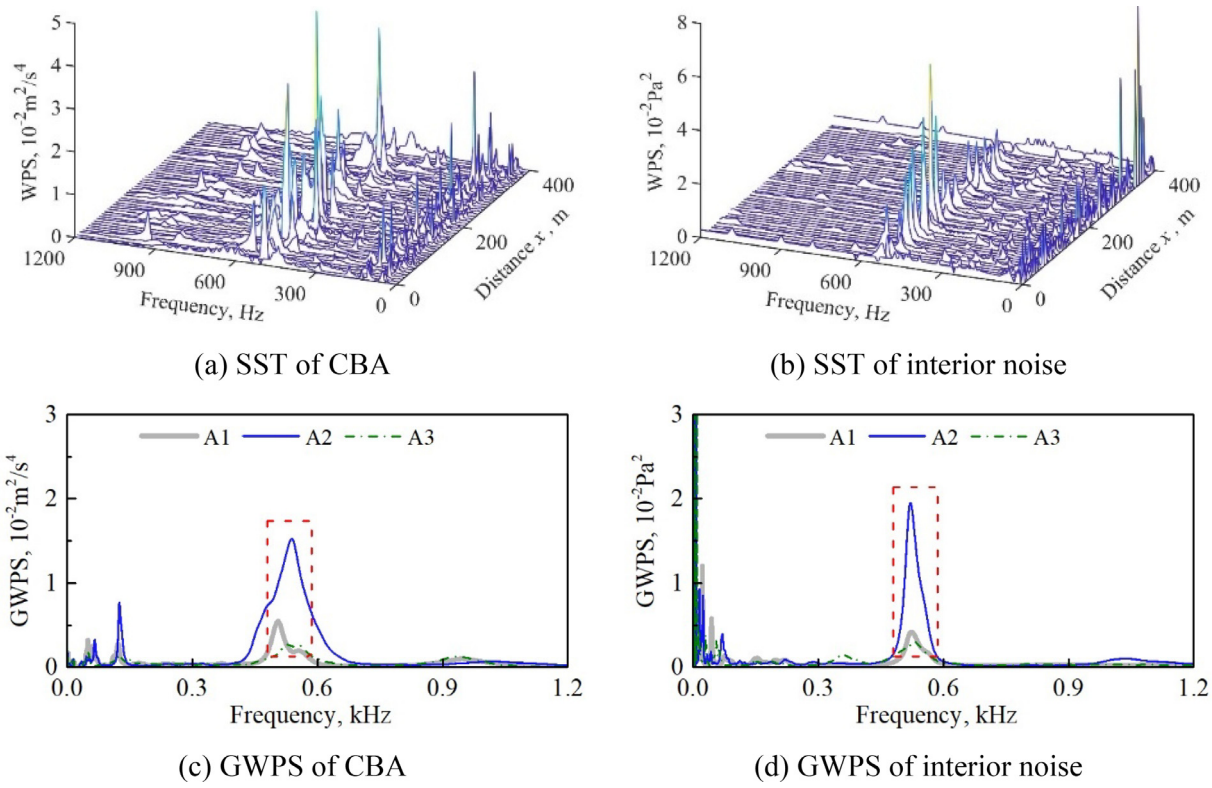

Fig. 6. Time-frequency distributions of the carriage interior responses on the sharp curve of the HSR track A.

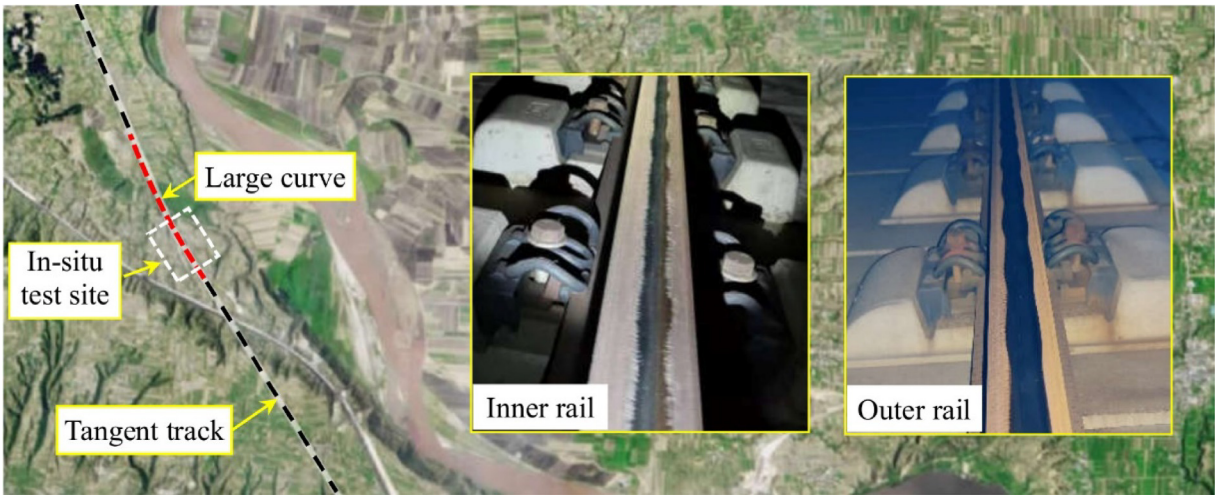

Fig. 7. Rail corrugation on the large curve of the HSR track B.

corrugation. Therefore, the capability of only the carriage interior noise is investigated for the inspection of rail corrugation in the next step.

Table 1 further compares the distributions of SAWP between the interior noise and ABA. For illustration purposes, a threshold of 2 is specified for the normalized SAWP, so that the positions with rail corrugation (the shadow region in Fig. 11) can be picked up, namely P_A^{SP} and P_A^{ABA} on the HSR track A as well as P_B^{SP} and P_B^{ABA} on the HSR track B. On the HSR track A, the wavelength of rail corrugation extracted from the interior noise is 59 mm, which is identical to the value from ABA. On the HSR track B, the wavelength from the interior noise is 131 mm, which is 2 mm smaller than that from ABA. Regarding the identified length of the degraded section, the deviation between the two signals is 21 m on HSR track A, and enlarges to 99 m on HSR track B.

As indicated in Fig. 11 and Table 1, the time–frequency distributions of carriage interior noise show a good agreement with the ABA signals under different train speeds and with different tracks radii. Compared with the ABA measurement, the acquisition of carriage interior noise does not rely on complex instrumentation on the running gear, which could be more convenient for the application on operational vehicles.

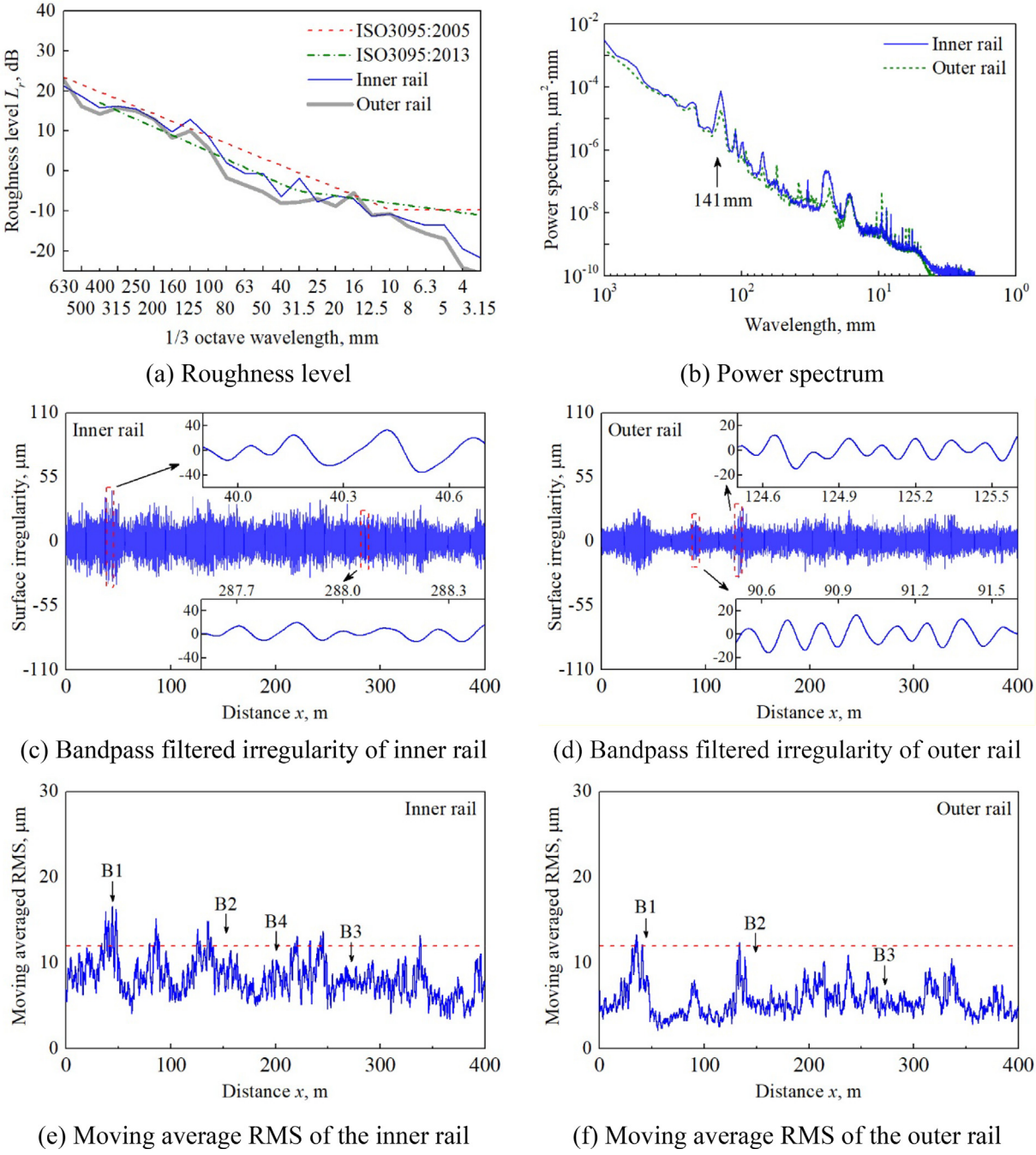

Fig. 8. Rail surface irregularity on the large curve of the HSR track B.

4. Trial inspection and verification

In this section, the characteristics of the corrugation-induced carriage interior noise are employed to develop an on-board inspection algorithm, which is then demonstrated on a third HSR track with an unknown rail surface condition.

4.1. Inspection algorithm

As shown in Section 3.1, the measured rail corrugation promotes the energy of the interior noise concentrated at 500 ~ 550 Hz on the HSR track A and 550 ~ 650 Hz on the HSR track B. In the inspection algorithm, the concerned frequency range is extended to 400 ~ 700 Hz, to account for more generalized scenarios with various combinations of rail corrugation geometry and train speed. Note that the specified frequency range may not cover all the potential rail corrugation types and train operation conditions on the HSR track, whereas the further enlargement of the concerned frequency range may affect the accuracy of the inspection. The inspection procedure is proposed as follows:

- Divide the measured carriage interior noise signal $f(t)$ into each moving window$k$, with the window length being T_W and the time shift between adjacent windows beingT_F, respectively.
- For each window$k$, calculate the ratio of the SAWP at 400 ~ 700 Hz using Equation (2). In the step, the ratio of the SAWP is employed instead of the SAWP itself, to reduce the influence of train speed variation on the energy concentration [34] and further on the anomaly identification.

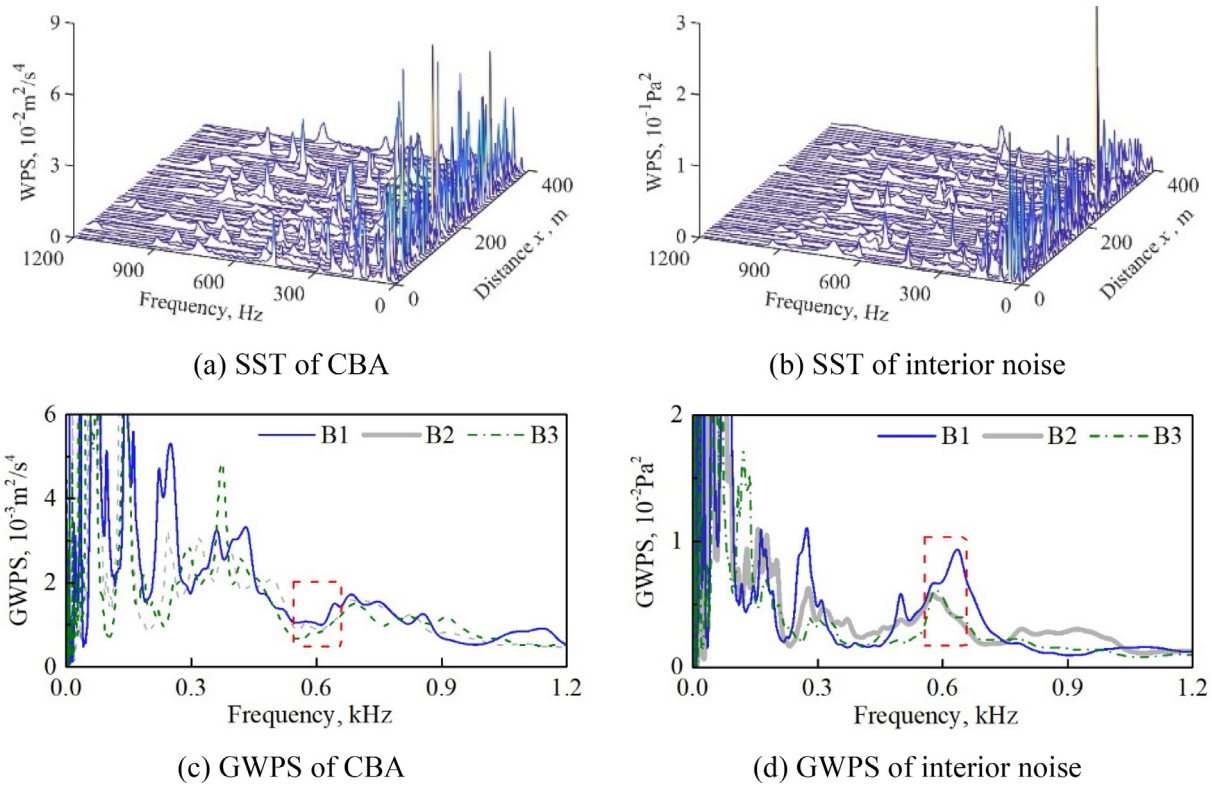

Fig. 9. Time-frequency distributions of the carriage interior responses on the large curve of the HSR track B.

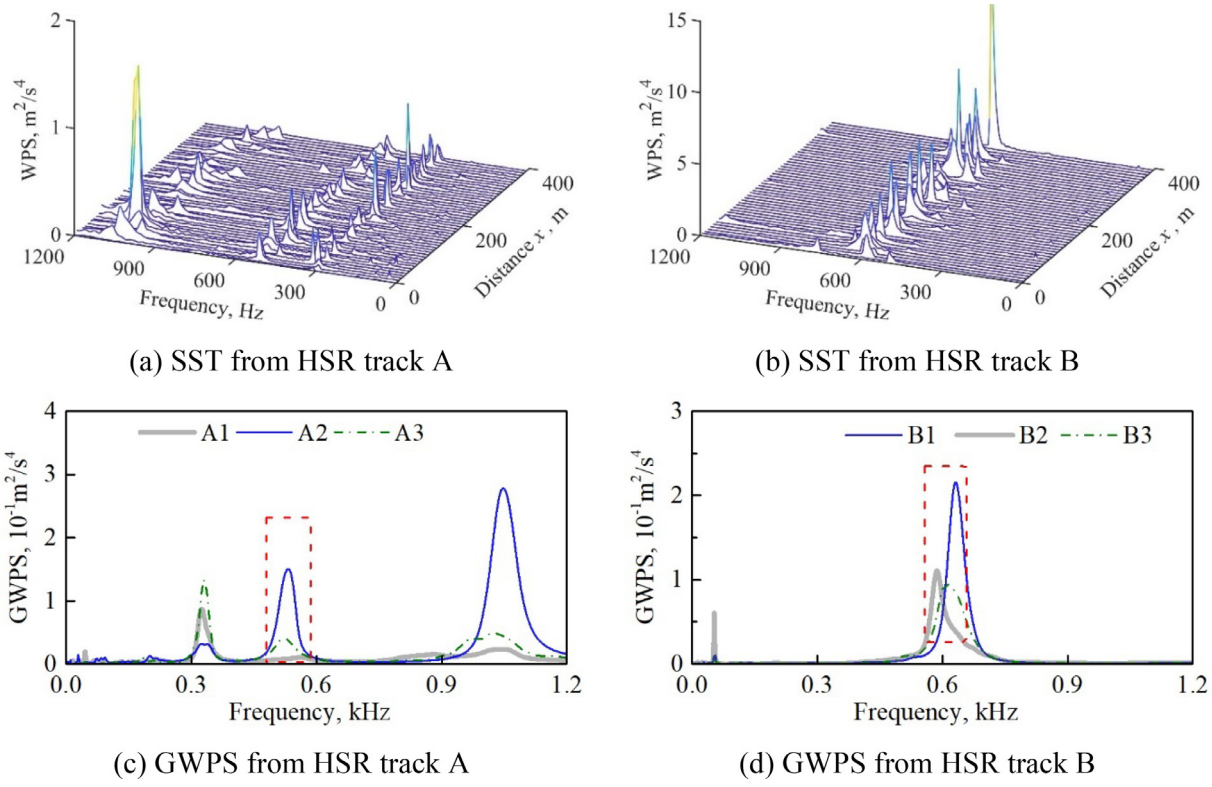

Fig. 10. Time-frequency distributions of the measured ABA signals.

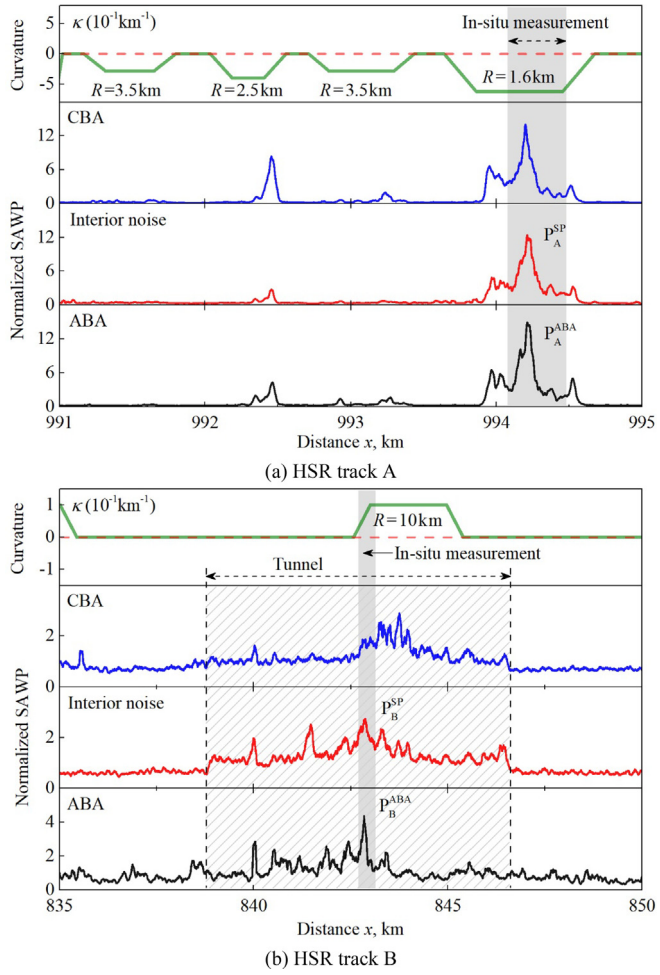

Fig. 11. Comparison of SAWP between different vehicle response signals.

$$\Delta T_W^k[400,700] = \frac{T_W^k[400,700]}{T_W^k[0,f_s/2]} \tag{8}$$

where f_s is the sampling frequency of the measured item.

- Calculate the nondimensional rail corrugation index I_C in each window via:

$$I_C(k) = \frac{N_k \Delta T_W^k[400,700]}{\sum_{k=1}^{N_k} \Delta T_W^k[400,700]} \tag{9}$$

where the N_k is the number of the moving window within the whole measured period.

- Identify the regions with a value of I_C higher than the threshold I_T, which can be regarded as the track sections with rail corrugation. Note that the threshold I_T is determined based on trial inspections and engineering judgment, and may differ from one track to another.
- For each identified window, calculate the power spectrum density (PSD) and then extract the typical wavelength of corrugation under the specified train speed.

4.2. Trial inspection via operational train

The proposed algorithm is demonstrated on the HSR track C with an unknown rail surface condition. The train-borne measurement was conducted using the operational train, see Fig. 2. The length of the train-borne measurement is 80 km, and the train speed varies significantly from 44 km/h to 346 km/h during the measurement. In the inspection algorithm, the values of T_W, T_F and I_T are set to 2 s, 0.5 s and 2, respectively. Fig. 12 gives the distribution of the rail corrugation index I_C on the HSR track C. For illustration purposes, the track curvature and train speed are attached. In Fig. 12(a), the rail corrugation index I_C exceeds the threshold I_T at two regions, i.e., C1 and C2. Both the two regions are located on tangent tracks, where the train speeds are 116 km/h and 161 km/h, respectively. Regarding the identified wavelengths, they are 51 mm and 104 mm at C1 with the latter being dominant (Fig. 12(b)), and the value shifts to 73 mm at C2 (Fig. 12(c)).

4.3. Verification via in-situ measurements

To examine the performance of the inspection algorithm, in-situ measurement of rail surface irregularity was conducted at track site C1, whereas site C2 is inaccessible due to safety regulations. Fig. 13 gives the photo captured at C1. The observed anomaly initiates from an improper rail grinding strategy, and the rail surface contains several periodic irregularity components with different wavelengths. This is confirmed by the roughness level of the measured rail surface irregularity, see Fig. 13(b). At the 1/3 octave wavelength of 100 mm, the roughness level on the right rail reaches 19.3 dB, which is 14.4 dB higher than the limit of Standard ISO 3095:2013. At the 1/3 octave wavelength of 50 mm, the roughness level is 2.3 dB on the left rail and 4.9 dB on the right rail, both of them exceed the limit of −1.1 dB.

As shown in Fig. 12 ~ 13, the proposed inspection algorithm demonstrates its capability in identifying the position and typical wavelength of rail corrugation. Besides, its performance is not affected much by the large variation in train speed. In this study, the concerned frequency range is extracted from the case studies in Section 3 and locates at 400 ~ 700 Hz, and the inspection algorithm is designed by identifying the time–frequency distributions of these characteristic frequencies. Because of the complicated initiation mechanisms and influencing factors of rail corrugation [1,35], the geometry of rail corrugation and the inspection speed may vary in a wider range. This will affect the parameter

Table 1
Comparison of the SAWP between interior noise and ABA.

HSR Track	Measured item	Identified section of rail corrugation				Typical wavelength (mm)
		Tag	Starting point (km)	Endpoint (km)	Length (m)	
A	Interior noise	P_A^{SP}	993.930	994.532	602	59
	ABA	P_A^{ABA}	993.926	994.550	624	59
B	Interior noise	P_B^{SP}	843.334	844.032	698	131
	ABA	P_B^{ABA}	843.261	844.058	797	133

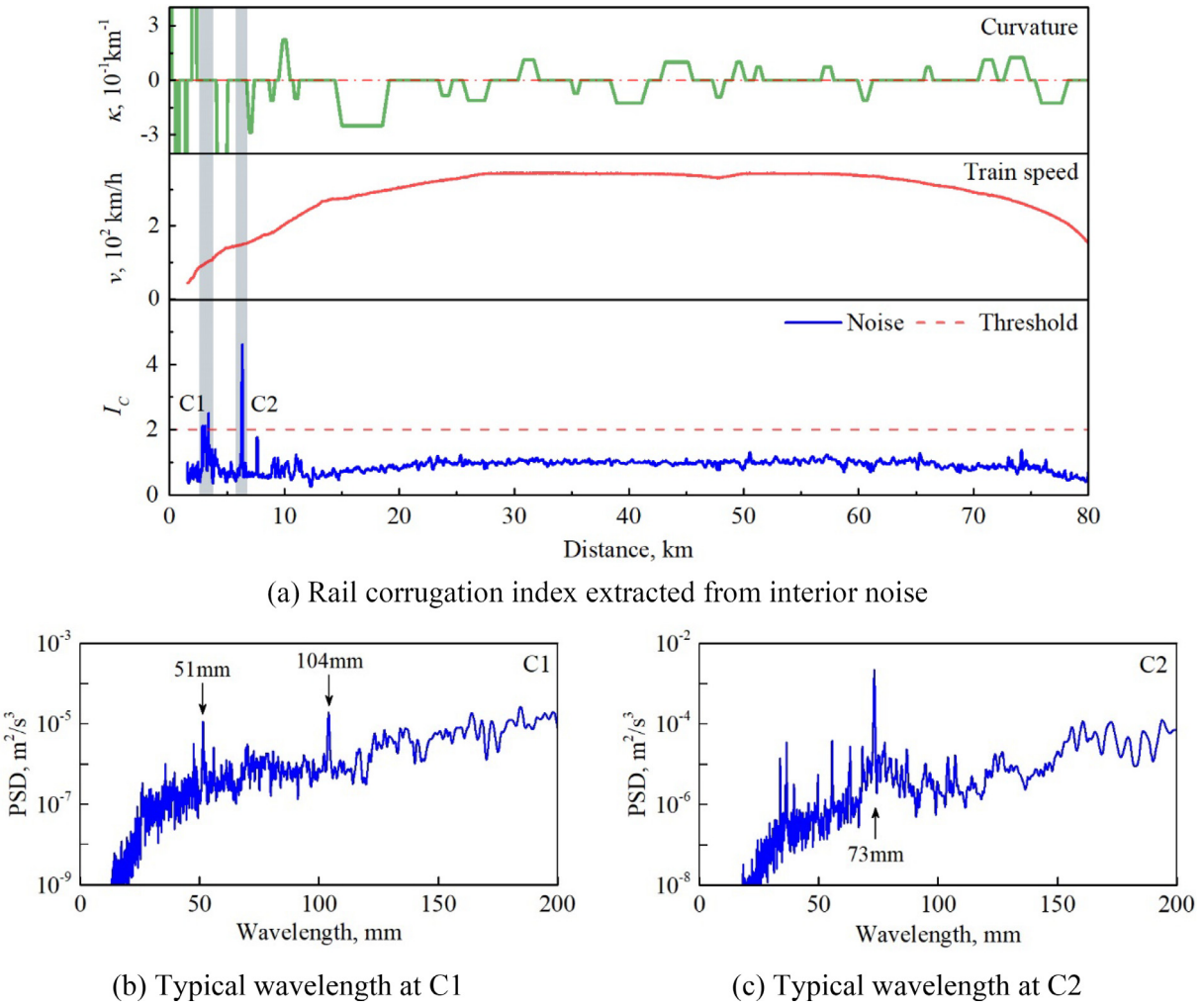

Fig. 12. Trial inspection results on the HSR track C.

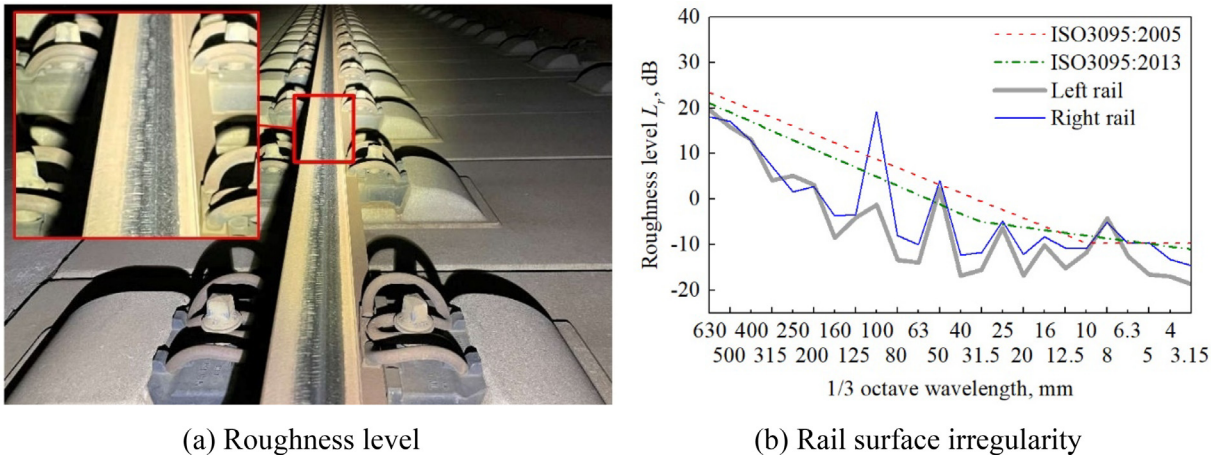

Fig. 13. Verification of rail surface irregularity at the track site C1.

determination of the inspection algorithm, such as passband, window length, and critical threshold. This will be done by investigating the corrugation-induced carriage interior responses under more generalized scenarios, so that the capability and accuracy of the proposed algorithm can be improved. Note that the following factors may affect the performance of the proposed method: First, the disturbances from vehicle anomalies, such as the wheel out-of-roundness, bolt looseness within the carriage, and door

shaking of the driver's cage, Second, the inherent geometric and stiffness irregularity of railway tracks, i.e, the turnout, transition zone, and insulated rail joint. Third, the significant and sudden changes in train operation conditions, such as abrupt deceleration and extreme crosswind.

5. Discussion: Measures to improve the capability of corrugation inspection

5.1. Speed dependency of rail corrugation index

As shown in Fig. 12(a), the rail corrugation index I_C is not speed independent, that is, the index raises slightly with the train speed in the regions without rail corrugation. The speed dependency of the index may affect the accuracy of corrugation inspection. This problem may be overcome by introducing a speed-dependent parameter in Equation (9), which indicates the relation between the train speed and the power spectrum of interior noise at a specified frequency range. The speed-dependent parameter can be extracted by either interior noise measurements (e.g., Fig. 4 in Qian et al. [34]) or numerical simulations (e.g., Fig. 6 in Molodova et al. [36]).

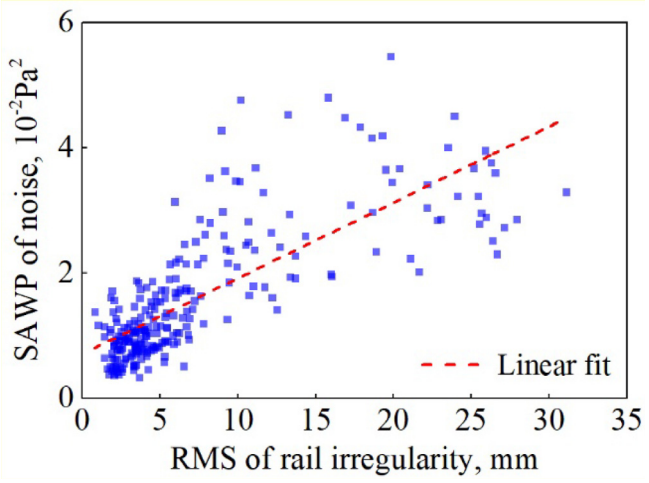

Fig. 14. Relation between the measured rail irregularity and interior noise on the HSR track A.

5.2. Estimation of rail corrugation amplitude

In Section 4, the proposed inspection algorithm shows the capability of identifying the regions with relatively significant corrugation. Yet, it remains unclear regarding the exact corrugation amplitude via interior noise measurement. Take the HSR track A for example, Fig. 14 gives the distribution of interior noise under different rail irregularities. In the figure, the RMS of the filtered rail surface irregularity with the passband of 30 ~ 100 mm as well as the corresponding SAWP of interior noise at 400 ~ 700 Hz is plotted. For comparison purposes, a window length of 1.5 m, referred from Standard EN 13231–3:2006, is specified for both the irregularity and response signals. As can be seen, the SAWP generally raises with the increased irregularity amplitude, and Pearson's correlation coefficient reaches 0.78. Furthermore, the amplitude of rail corrugation can then be estimated if the correlation between the excitation and the response is extracted under a wide variation of train speed (e.g., 40 ~ 350 km/h) via either the train-borne & in-situ measurements or numerical simulations.

In addition, it is noted that the threshold of the rail corrugation index (i.e., 2 in Section 4.2) does not have a physical basis, e.g., the lower bound of corrugation amplitude or the limits from Standards ISO3095 & EN 13231. The analysis of the correlation between the excitation and the response can also contribute to optimizing the threshold.

5.3. Processing method of the noise signal

In general, the simple sound pressure level-based analysis (e.g., the sound pressure level within a specified frequency band) is also able to evaluate the corrugation-induced noise response. In this study, we use the wavelet-based approach rather than the sound pressure level-based approach, mainly due to the proposed wavelet-based approach being able to capture the instantaneous frequency characteristics. With the sampling frequency of 5 kHz, the analyzed track length can be as short as 0.02 m under the train speed of 300 km/h. Yet, within such a short track length, is not able to conduct the conventional spectrum analysis of sound pressure levels. For example, the number of sampling points should be longer than 1 s, so that the track length should be at least 30 m under train speed of 110 km/h and raises to 83 m under train speed of 300 km/h. Therefore, the typical corrugation wavelength within a short track length can be extracted.

Fig. 15 compares the performance of the preceding two methods for the HSR track A. In Fig. 15(a), the track length is set to

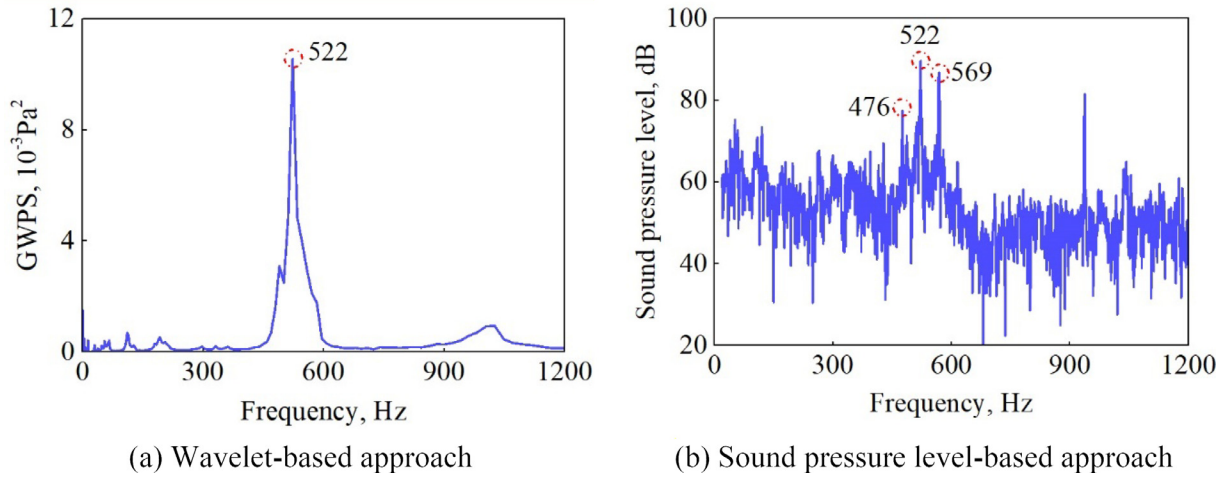

(a) Wavelet-based approach (b) Sound pressure level-based approach

Fig. 15. Comparison of different noise processing methods.

1 m (994.150 ~ 994.151 km), in which there only exists 164 sampling points under the train speed of 110 km/h, and the typical frequency of 522 Hz (the corresponding corrugation wavelength is 58 mm) is successfully identified. In Fig. 15(b), the track length is set to 30 m (994.150 ~ 994.180 km) and contains 5000 sampling points, which is a minimum level for the sound pressure level analysis. In the figure, several typical frequencies, e.g., 522 Hz, 476 Hz and 569 Hz are picked up. In such a case, it is difficult to capture the dominant corrugation wavelength at a shorter track length.

5.4. Capability for more generalized scenarios

Based on the proposed train-borne measurement device, a mass of carriage interior noise signals has been collected under more generalized scenarios, in which the variations of vehicle type (including CRH400BF, CRH380A, CRH380B, and CRH2), maximum train speed (from 250 km/h to 350 km/h), and track structure (including ballast track, slab ballastless track and Bi-block ballastless track) were taken into account. Yet, due to the strict safety regulations of the HSR authority as well as the strict anti-epidemic of COVID measures, the chances to get access to the HSR tracks are very limited. We plan to do so when the anti-epidemic measures loose, so that we list this part in the further work.

In further work, more in-situ tests will be conducted, so that the characteristics of corrugation-induced carriage interior noises can be extracted under more generalized scenarios. The gained information is beneficial to adopt the inspection algorithm to a wider variety of inspection conditions. Meanwhile, the capability of the proposed inspection method will be investigated in identifying other vehicle and track defects, such as wheel out-of-roundness and worn insulated rail joints, so that the health condition of HSR tracks can be monitored in a timely fashion.

6. Conclusions

This study proposes an indirect inspection method for rail corrugation on HSR tracks via carriage interior noise. For this purpose, train-borne vibration & noise measurements were integrated with in-situ rail surface irregularity tests, to extract the characteristic carriage interior responses induced by rail corrugation. The time–frequency distributions of interior noise were identified, and then employed to design the inspection algorithm. Thereafter, the proposed algorithm was demonstrated on a third HSR track with an unknown rail surface condition. The main conclusions are drawn as follows:

(1) The presence of rail corrugation measured on both the sharp and large curves aggravates the carriage interior noise at the frequency range of 400 ~ 700 Hz, and the energy concentration raises with the exacerbation of rail corrugation.
(2) The car body acceleration induced by rail corrugation on the sharp curve coincides well with the axle box acceleration in both time and frequency domains, whereas it fails in capturing both the characteristic frequency components and the exact position of rail corrugation on the large curve.
(3) The energy of the carriage interior noise concentrated at 400 ~ 700 Hz raises during the passage of the high-speed train over the tunnel, while the phenomenon is not obvious for both car body and axle box acceleration signals.
(4) The carriage interior noise demonstrates its capability in identifying the position, typical wavelength, and severity of rail corrugation under inconstant train speed conditions, and its performance is confirmed by the widely-recognized axle box acceleration measurements.

CRediT authorship contribution statement

Zilong Wei: Conceptualization, Formal analysis, Methodology, Writing – original draft, Writing – review & editing. **Xianfu Sun:** Data curation, Software, Validation. **Fei Yang:** Conceptualization, Methodology, Writing – review & editing. **Zaitian Ke:** Funding acquisition, Project administration, Resources. **Tao Lu:** Formal analysis, Writing – review & editing. **Pan Zhang:** Formal analysis, Software. **Chen Shen:** Methodology, Software, Writing – original draft, Writing – review & editing.

Declaration of Competing Interest

The authors declare that they have no known competing financial interests or personal relationships that could have appeared to influence the work reported in this paper.

Acknowledgements

This study is supported by the Scientific Research Plan of China Railway No. P2021T013 as well as the Science and Technology Research Plan of China Academy of Railway Sciences No. 2021YJ022.

References

[1] Grassie SL. Rail irregularities, corrugation and acoustic roughness: characteristics, significance and effects of reprofiling. Proc Inst Mech Eng, Part F: J Rail Rapid Transit 2012;226(5):542–57.
[2] Liu W, Zhang H, Liu W, Thompson DJ. Experimental study of the treatment measures for rail corrugation on tracks with Egg fasteners in the Beijing metro. Proc Inst Mech Eng, Part F: J Rail Rapid Transit 2018;232(5):1360–74.
[3] Tanaka H, Miwa M. Modeling the development of rail corrugation to schedule a more economical rail grinding. Proc Inst Mech Eng, Part F: J Rail Rapid Transit 2020;234(4):370–80.
[4] Oostermeijer KH. Review on short pitch rail corrugation studies. Wear 2008;265(9-10):1231–7.
[5] Liu X, Han J, Xu H, Xiao X, Wen Z, Liang S. An indirect method for rail corrugation measurement based on numerical models and wavelet packet decomposition. Measurement 2022;191:110726.
[6] Sadeghi J, Hasheminezhad A. Correlation between rolling noise generation and rail roughness of tangent tracks and curves in time and frequency domains. Appl Acoust 2016;107:10–8.
[7] Cui X, He Z, Huang B, Chen Y, Du Z, Qi W. Study on the effects of wheel-rail friction self-excited vibration and feedback vibration of corrugated irregularity on rail corrugation. Wear 2021;477:203854.
[8] Grassie SL. A practical methodology to prioritise reprofiling sites for corrugation removal. Proc Inst Mech Eng, Part F: J Rail Rapid Transit 2020;234(4):362–9.
[9] Kang G, Gao S, Yu L, Zhang D. Deep architecture for high-speed railway insulator surface defect detection: denoising autoencoder with multitask learning. IEEE Trans Instrum Meas 2019;68(8):2679–90.
[10] Pieringer A, Kropp W. Model-based estimation of rail roughness from axle box acceleration. Appl Acoust 2022;193:108760.
[11] Teng Y, Liu H, Liu J, Wang C, Ma Z. A rail corrugation measurement method based on data splicing. Measurement 2020;156:107560.
[12] Gazafrudi SMM, Younesian D, Torabi M. A high accuracy and high speed imaging and measurement system for rail corrugation inspection. IEEE Trans Ind Electron 2021;68(9):8894–903.
[13] Li Q, Shi Z, Zhang H, Tan Y, Ren S, Dai P, et al. A cyber-enabled visual inspection system for rail corrugation. Fut Gener Comput Syst 2018;79:374–82.
[14] Grassie SL. Routine measurement of long wavelength irregularities from vehicle-based equipment. Noise and Vibration Mitigation for Rail Transportation Systems: Springer; 2018; 333-342.
[15] Salvador P, Naranjo V, Insa R, Teixeira P. Axlebox accelerations: Their acquisition and time–frequency characterisation for railway track monitoring purposes. Measurement 2016;82:301–12.
[16] Shadfar M, Molatefi H. Detection of rail local defects using in-service trains. Proc Inst Mech Eng, Part F: J Rail Rapid Transit 2022. DOI: 10.1177/09544097221076253.
[17] Oregui M, Li S, Núñez A, Li Z, Carroll R, Dollevoet R. Monitoring bolt tightness of rail joints using axle box acceleration measurements. Struct Control Health Monit 2017;24(2):e1848.
[18] Zoccali P, Loprencipe G, Lupascu RC. Acceleration measurements inside vehicles: Passengers' comfort mapping on railways. Measurement 2018;129:489–98.

[19] Rodríguez A, Sañudo R, Miranda M, Gómez A, Benavente J. Smartphones and tablets applications in railways, ride comfort and track quality. Transition zones analysis. Measurement 2021;182:109644.
[20] Azzoug A, Kaewunruen S. RideComfort: a development of crowdsourcing smartphones in measuring train ride quality. Front Built Environ 2017;3:3.
[21] Cong J-l, Gao M-Y, Wang Y, Chen R, Wang P. Subway rail transit monitoring by built-in sensor platform of smartphone. Front Inf Technol Electron Eng 2020;21(8):1226–38.
[22] Tanaka H, Shimizu A. Practical application of portable trolley for the continuous measurement of rail surface roughness for rail corrugation maintenance. Quart Rep RTRI 2016;57:118–24.
[23] Han J, Xiao X, Wu Y, Wen Z, Zhao G. Effect of rail corrugation on metro interior noise and its control. Appl Acoust 2018;130:63–70.
[24] Kim H, Hu Z, Thompson D. Numerical investigation of the effect of cavity flow on high speed train pantograph aerodynamic noise. J Wind Eng Ind Aerodyn 2020;201:104159.
[25] Li L, Cai H, Han H, Jiang Q, Ji H. Adaptive short-time Fourier transform and synchrosqueezing transform for non-stationary signal separation. Signal Process 2020;166:107231.
[26] Daubechies I, Lu J, Wu H-T. Synchrosqueezed wavelet transforms: an empirical mode decomposition-like tool. Appl Comput Harmon Anal 2011;30 (2):243–61.
[27] Cohen MX. A better way to define and describe Morlet wavelets for time-frequency analysis. NeuroImage 2019;199:81–6.
[28] Santos CAG, Guerra-Gomes IC, Gois BM, Peixoto RF, Keesen TSL, da Silva RM. Correlation of dengue incidence and rainfall occurrence using wavelet transform for João Pessoa city. Sci Total Environ 2019;647:794–805.
[29] ISO 3095-2013. Acoustics - Railway applications - Measurement of noise emitted by railbound vehicles. International Organization for Standardization; 2013.
[30] EN 13231-3:2006. Railway applications of rail grinding, milling and planning work in tracks. European Committee for Standardization; 2006.
[31] Grassie SL. Rail corrugation: characteristics, causes, and treatments. Proc Inst Mech Eng, Part F: J Rail Rapid Transit 2009;223(6):581–96.
[32] Park B, Jeon J-Y, Choi S, Park J. Short-term noise annoyance assessment in passenger compartments of high-speed trains under sudden variation. Appl Acoust 2015;97:46–53.
[33] Soeta Y, Shimokura R. Survey of interior noise characteristics in various types of trains. Appl Acoust 2013;74(10):1160–6.
[34] Qian K, Hou Z, Sun Q, Gao Y, Sun D, Liu R. Evaluation and optimization of sound quality in high-speed trains. Appl Acoust 2021;174:107830.
[35] Matsumoto A, Sato Y, Ono H, Tanimoto M, Oka Y, Miyauchi E. Formation mechanism and countermeasures of rail corrugation on curved track. Wear 2002;253(1-2):178–84.
[36] Molodova M, Li Z, Nunez A, Dollevoet R. Parameter study of the axle box acceleration at squats. Proc Inst Mech Eng, Part F: J Rail Rapid Transit 2014; 229: 841-851.